

Local symmetry breaking and orbital glass behaviour in CoFe_2O_4

Soumya Shephalika Behera,¹ Isha,¹ Arvind Kumar Yogi,¹ V R Rao Medicherla,^{2,*} Parasmani Rajput,³ Archana Sagdeo,^{4,5} Jaspreet Singh,⁴ Vasant Sathe,¹ and R J Choudhary^{1,†}

¹*UGC-DAE Consortium for Scientific Research, Indore 452001, India*

²*Department of physics, ITER, Siksha 'O' Anusandhan Deemed to be University, Bhubaneswar 751030, India*

³*Beamline Development and Application Section,*

Bhabha Atomic Research Centre, Trombay, Mumbai 400085, India

⁴*Accelerator Physics and Synchrotrons Utilization Division,*

Raja Ramanna Centre for Advanced Technology, Indore 452017, India

⁵*Homi Bhabha National Institute, Training School Complex, Anushakti Nagar, Mumbai 400094, India*

(Dated: June 23, 2025)

The structural distortions, orbital correlations, and electronic states in cobalt ferrite (CoFe_2O_4) were investigated using complementary characterisation techniques, including synchrotron X-ray diffraction (SR-XRD), hard X-ray photoelectron spectroscopy (HAXPES), X-ray absorption spectroscopy (XANES), extended X-ray absorption fine structure (EXAFS), and Raman spectroscopy. SR-XRD confirms phase purity and reveals a temperature-dependent superlattice reflection between 200 K and 100 K, consistent with the emergence of short-range orbital ordering driven by cooperative Jahn-Teller distortion (JTD). The disappearance of this feature below 100 K signals orbital freezing and the onset of a glass-like orbital state. HAXPES measurements show multiplet splitting and charge-transfer satellite features in the Co and Fe $2p$ core levels, indicating mixed valence states and strong electron correlations. XANES analysis reveals hybridized p - d states and local coordination distortions. Temperature-dependent EXAFS measurements indicate increasing local disorder—particularly in Fe–O and Fe–Fe octahedral bonds—as evidenced by enhanced Debye–Waller factors. These distortions, attributed to cation redistribution and oxygen vacancies, are static and asymmetric, primarily affecting the octahedral sublattice. Notably, signatures of cooperative Jahn-Teller distortions emerge in the intermediate temperature range ($T_o \approx 200$ – 100 K) and disappear upon further cooling. Raman spectroscopy further supports these findings, revealing phonon anomalies and enhanced spin-phonon coupling in the same temperature range. Magnetic measurements indicate spin reorientation and exchange interaction anomalies that align with the orbital behaviour. Together, these results hint at a frustrated orbital state in CoFe_2O_4 —possibly involving cooperative Jahn-Teller distortions, disrupted long-range coherence, and orbital glass behaviour—offering new insights into the coupling of orbital, spin, and lattice degrees of freedom in spinel systems.

Keywords: EXAFS, Debye waller factor, shake-up satellite, magnetoelastic coupling

INTRODUCTION

Transition metal oxides with partially filled d -orbitals exhibit a rich of electronic, magnetic, and structural phenomena due to the strong interplay among charge, spin, orbital, and lattice degrees of freedom [1, 2]. Among these, the orbital degree of freedom—arising from the spatial orientation of degenerate d -orbitals—plays a pivotal role in determining the ground state properties of many correlated systems [2, 3].

Orbital ordering, typically stabilized by cooperative JTD, lifts the degeneracy of the e_g orbitals, leading to symmetry-lowering structural transitions and the emergence of long-range ordered phases. This mechanism is well documented in systems such as LaMnO_3 [4–6], KCuF_3 [3], and spinel ferrites containing Mn^{3+} and Cu^{2+} ions, where JT distortions are intimately linked to magnetic anisotropy and structural instabilities.

However, in systems with inherent site disorder, geometric frustration, or competing interactions, the development of long-range orbital ordering can be hindered.

Instead, such materials may enter a frozen, disordered state known as the orbital glass [1]. In this state, while local orbital distortions persist due to strong JT coupling, their spatial correlations remain short-ranged and frustrated, preventing global symmetry breaking. The orbital glass state is thus characterized by static but spatially random orbital orientations [1], reflecting a delicate balance between ordering tendencies and frustration effects. Understanding the emergence and stabilization of such glassy orbital states is essential for elucidating exotic ground states in correlated oxides.

AB_2O_4 is a spinel type structure and the magnetic and electrical properties of spinels depend on cations distribution in the tetrahedral (A) and octahedral (B) sublattices of a cubic structure. In particular CoFe_2O_4 ferrite is a very important spinel type structure with ferrimagnetic behavior (high Curie temperature $T_c = 793$ K), strong magnetocrystalline anisotropy along with a moderate magnetization (M_s), and high coercivity (H_c) [1, 7]. Thus, CoFe_2O_4 , a classic inverse spinel ferrite, serves as a compelling system for investigating the interplay between lattice distortions, orbital degrees of freedom, and

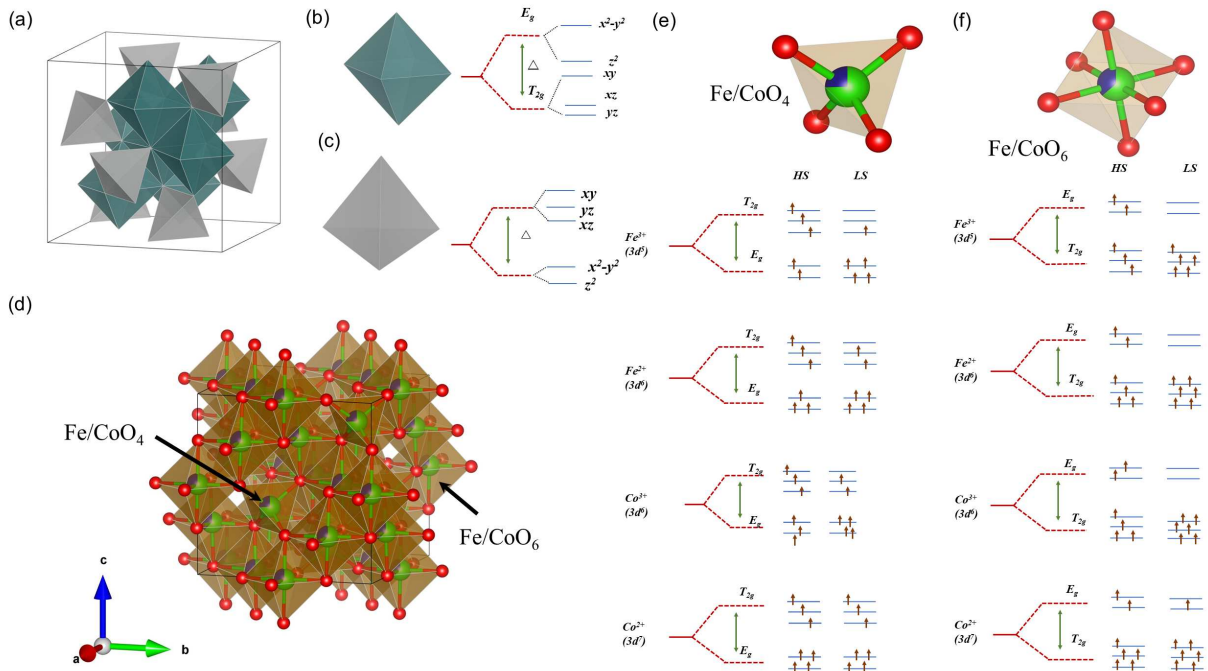


FIG. 1. (a) Schematic of the spinel lattice showing two distinct crystallographic sites: tetrahedral and octahedral. (b, c) Schematic diagrams of crystal electric field (CEF) splitting and orbital configurations in tetrahedral and octahedral environments. (d) Crystal structure of CoFe₂O₄ projected onto the bc -plane. (e) CEF splitting and orbital degeneracy in the distorted CoO₄/FeO₄ tetrahedral units and (f) in the CoO₆/FeO₆ octahedral environment, both influenced by the Jahn–Teller (J–T) effect.

magnetic behavior. In its inverse spinel structure, Co²⁺ ions predominantly occupy octahedral sites, while Fe³⁺ ions are distributed across both tetrahedral and octahedral positions. The partial cation inversion and competition between crystal field splitting, Hund’s exchange interactions give rise to complex magnetic anisotropy and orbital-lattice coupling.

The electronic configurations of transition-metal cations in octahedral coordination play a crucial role in driving local structural distortions via the Jahn–Teller (JT) effect. In CoFe₂O₄, Co²⁺ (3d⁷) and Fe³⁺ (3d⁵) ions occupy octahedral sites in a partially inverse spinel structure. High-spin Co²⁺ adopts a $t_{2g}^5 e_g^2$ configuration and is a JT-active ion, as the system can lower its energy through local lattice distortions that will lift the t_{2g} orbital degeneracy. While Fe³⁺ in the high-spin 3d⁵ configuration is typically considered JT-inactive. A schematic of the spinel lattice with tetrahedral and octahedral sites, their crystal field splitting and orbital degeneracy, along with the crystal structure of CoFe₂O₄ projected onto the bc -plane, is shown in Fig. 1(a–e).

The coexistence of JT-active (Co²⁺, Fe²⁺) and non-JT-active (Fe³⁺) ions, coupled with cationic inversion and mixed valence states, leads to a spatially inhomogeneous distortion field. However, the origin of such local structural distortion is still not explained which is crucial to understand its electronic properties. These distur-

tions remain local and dynamically fluctuating, preventing the development of long-range orbital order. Instead, short-range orbital correlations emerge in the intermediate temperature range[8], which ultimately freeze into a disordered, non-periodic orbital configuration at low temperatures—indicative of an orbital glass state. Such microscopic details for interesting bulk Cobalt-ferrite CoFe₂O₄ is crucial and we believe that effect of Co and Fe local environment plays an important role in the physical properties which we address by using detailed local probe techniques. For instance EXAFS render several important information on interplay between spin state, orbital degeneracy, and local symmetry-breaking arising due to the cooperative JT distortions as we qualitatively explain in Fig. 1. These crucial information about the local bond-distances and the effective coordination numbers of neighboring atoms can help to understand the physical properties of CoFe₂O₄ in great detail. And thus we design our present study by focusing on local probes techniques such as X-ray absorption spectroscopy (XANES) and extended X-ray absorption fine structure (EXAFS) to capture the local symmetry-breaking which significantly influence the Co and Fe spin states in CoFe₂O₄.

In this study, we investigate the structural and electronic properties of CoFe₂O₄ (CFO), with a particular focus on the role of crystal distortions in shaping its magnetic and electronic behavior. X-ray absorption spec-

troscopy (XAFS) is employed to probe the local electronic environments of Co and Fe ions, while extended X-ray absorption fine structure (EXAFS) analysis provides insights into their local coordination and atomic structure. The EXAFS data, analyzed using the Debye–Waller factor within the correlated Einstein model, reveal temperature-dependent lattice disorder and the presence of Jahn–Teller distortions (JTD). Hard X-ray photoelectron spectroscopy (HAXPES) measurements at room temperature further confirm the chemical states and mixed valence character of the cations, as well as the presence of charge transfer satellite features, reflecting crystal field effects and electronic correlations.

Synchrotron X-ray diffraction (SR-XRD) is used to examine the long-range crystallographic structure. While the global cubic symmetry remains intact, a distinct superlattice reflection appears between 200 K and 100 K. Complementary Raman spectroscopy supports these findings, revealing a pronounced softening of the E_g phonon mode—consistent with enhanced orbital–lattice coupling and the onset of short-range orbital correlations. Magnetic measurements additionally indicate spin ordering in the same temperature regime, suggesting the emergence of exchange interactions coupled to the orbital [1].

EXPERIMENTS

Polycrystalline cobalt ferrite CoFe_2O_4 was synthesized by a conventional solid-state reaction route. The initial ingredients, Fe_2O_3 and CoO , were ground in stoichiometric amounts to create a homogeneous mixture. The mixture was then subjected to a 12-hour calcination process at 750°C and subsequently calcined at 900°C for 12 hours to synthesize the CoFe_2O_4 (CFO) sample.

X-ray Diffraction (XRD), X-ray Absorption Near Edge Structure (XANES), and Extended X-ray Absorption Fine Structure (EXAFS) as well as Hard X-ray Photoelectron Spectroscopy (HAXPS) measurements were carried out on CoFe_2O_4 using BL-12, and BL-09 and BL-14 beamlines respectively, at Indus-2 Synchrotron source at Raja Ramanna Center for Advanced Technology (RRCAT), Indore, India.

XRD measurements on CoFe_2O_4 powder were conducted in the temperature range of 50–300 K at the X-ray diffraction beamline (BL-12) of Indus-2 synchrotron utilizing an angle-dispersed setup with a MAR-345 Area detector. A uniform amount of finely grinded CoFe_2O_4 powder was deposited on Kapton tape and mounted on a liquid helium flow-type cryostat, placed on the Image plate sample holder setup. The diffraction geometry, including the sample-to-detector distance ($d = 200$ mm) and the perpendicularity of the detector to the X-ray beam, were calibrated by refining

the diffractograms of a reference LaB_6 sample, with an estimated wavelength of 0.63658 \AA . The 2D diffractograms were integrated using the FIT2D software to generate standard intensity versus 2θ 1D diffractograms. Full Debye ring integration from the 2D diffractograms ensured a high signal-to-noise ratio, which is particularly effective in revealing parasitic phases and minimizing the effects of privileged orientations, making the data ideal for structure refinement. Crystallographic structural parameters as a function of temperature were obtained by refining the 1D patterns using the full-profile Rietveld method in FULLPROF software.

The core levels of Co and Fe in CFO have been investigated using Hard X-ray Photo-Electron Spectroscopy (HAXPES) employing a photon energy of 4000 eV at beamline BL14 of the Indus-2 synchrotron. The vacuum in the analysis chamber was maintained in the 10^{-10} Torr range. The total resolution in the measurement was set to 0.8 eV to obtain a good signal-to-noise ratio. The surface cleaning procedures were purposefully avoided to prevent any surface damage that may induce extra features in photoemission. The binding energy of the photoelectrons was calibrated using 1s core level binding energy of contaminant carbon at 284.6 eV. This procedure for binding energy reference automatically compensates for any shift in binding energy due to the static charging of the sample during photoemission. During the measurement, no peak shift was observed between different scans, suggesting the absence of dynamic charging of the sample.

X-ray absorption spectroscopic data were recorded at the Fe and Co K-edges in transmission mode for all samples using the BL-09 beamline (4–25 keV) at the Indus-2 synchrotron source. The polycrystalline powder samples were mixed thoroughly with boron nitride (BN) using a mortar and pestle in proportions, ensuring that the absorption edge jump ($\Delta\mu$) ranged from 0.7 to 1, as calculated using the XAFSMASS code [9]. X-ray absorption fine-structure (XAFS) spectroscopy experiments were carried out in TEY mode using hard X-ray synchrotron radiation using Athena and Artemis software and X-ray absorption near-edge structure (XANES) and extended X-ray absorption fine-structure (EXAFS) spectral measurements in the energy range of 5 to 25 keV using BL-09 beamline of Indus-2 synchrotron.

Magnetization measurements were carried out with the help of the MPMS 7 T SQUID-VSM instrument (Quantum Design Inc., USA). Raman measurements were carried out using a Horiba JY HR-800 spectrometer equipped with excitation sources of 473 nm and 633 nm. The system employs an 1800 grooves/mm grating for spectral dispersion and a charge-coupled device detector for signal acquisition. Additionally, an external setup

was integrated to enable low-temperature measurements using liquid nitrogen up to 80K.

RESULTS AND DISCUSSION

Temperature-dependent XRD

To evaluate possibility of any structural symmetry-breaking transition in CoFe_2O_4 , we performed Temperature-dependent synchrotron X-ray diffraction (SR-XRD) measurements in the 300–50 K range. The detailed structural analysis by SR-XRD shows drastic change between 200 K and 100 K as shown in Fig. 2 (a). Temperature-dependent SR-XRD structural data analysis and the bond valence sum (BVS) calculation are performed by FullProf software [10]. The Rietveld refinement of one SR-XRD pattern at the room temperature (300 K) by the cubic $Fd-3m$ space group is shown in Fig. 2 (b). The lattice parameters at different temperatures were obtained by similar Rietveld refinement of the XRD patterns at different temperatures and were plotted in Fig. 2(c), and the insert showing the peak shifts progressively to higher angles with decreasing temperature, confirming lattice contraction.

Moreover, upon cooling, a distinct weak but pronounced peak possibly a super-lattice reflection, as shown in highlighted dashed line in Fig. 3 (a). It appears at $2\theta = 10.95$ degree, just below ~ 200 K, indicating the emergence of super-structure or lattice modulation in CFO. Interestingly the intensity of this peak increases with lowering temperature up to ~ 100 K, then it starts decreasing as shown in Fig. 3(b), possibly due to the development of strong short-range orbital correlations. Such orbital correlations may also break the symmetry and therefore our detailed temperature dependent SR-XRD suggesting a possible structural symmetry-breaking transition does exist in the temperature 200-100 K. It is in line with other measurements, as most of the physical and local probe low-temperature experiments on this compound show a clear change in this temperature interval only. Further, we try to include this super-lattice peak in our SR-XRD refinement as well under various lower symmetries of the inverse spinel CoFe_2O_4 structure by trial and error method for the automatic indexing of Powder diffraction patterns using DICVOL04 option of Fullprof software [10]. However, from our various attempts we could not successfully index the peak, most probably due to powder XRD averaging effect. X-ray diffraction of single-crystal thus would become crucial to explain this new super-lattice peak. From our try we at least found that the super-structure weak Bragg peak emerging at $2\theta = 10.95$ degree can be explained by $P4/mm$ symmetry, a simulated pattern with $P4/mm$ from LeBail fit

refinement is shown in Fig. 3 (c) and inset shows the super-lattice peak along with Bragg position. However, attempt to fully fit this super-lattice peak ($2\theta = 10.95$ degree) through either profile (LeBail-fit) or Rietveld refinement was failed [see inset of Fig. 3 (c)] and thus here we explain the emergence of this new super-lattice peak ($2\theta = 10.95$ degree) by an average structure analysis. This $P4/mm$ symmetry nicely explained rest all of the fundamental Bragg peaks as well [see Fig. 3 (c)], very similar to all the Bragg fundamental reflections as indexed by assuming the cubic space group $Fd-3m$, where all the crystallographic sites were fully occupied. However, with cubic space group $Fd-3m$ we found a drastic change in the super-structure region. The refined lattice parameters for high temperature phase with cubic space group $Fd-3m$ (no super structure) at 300 K are found to be $a = 8.381797(13)$ Å. However, at 155 K, without including super-structure, and considering only fundamental reflections, the lattice parameters are found to be $a = 8.3780037(16)$ Å. The crystal structure of CoFe_2O_4 for high temperature phase is shown in Fig. 1 (d). Moreover, an anomaly in the temperature dependent lattice parameter is observed in the temperature range of 100 to 200 K, as shown in Fig. 2 (c). Notably, Rietveld refinement confirms that the global symmetry remains cubic throughout, implying that the modulation originates from local JTD of the octahedra, rather than a long-range structural phase transition.

Below 100 K, the superlattice peak abruptly disappears [1], reflecting the breakdown of coherent orbital correlations. Instead of stabilizing into a long-range orbitally ordered phase, the system enters a frustrated, disordered regime where dynamic JT distortions freeze into a static configuration. The persistence of cubic symmetry and the disappearance of orbital modulation at low temperatures point toward the formation of an orbital glass state, characterised by randomly frozen orbital orientations and suppressed long-range order. These findings highlight the delicate interplay between orbital-lattice coupling and frustration, which can favour glassy freezing over conventional orbital ordering. To further investigate this phenomenon, we perform temperature-dependent Raman measurements, as presented below.

Raman Spectroscopy

Raman spectroscopy is a powerful tool for probing lattice dynamics and local structural changes in systems where spin, orbital, and lattice degrees of freedom are intertwined. In CoFe_2O_4 (CFO), deviations from the ideal spinel structure often activate additional Raman modes and lead to peak splitting, typically caused by crystal field effects, JTD, and cation disorder. These effects are

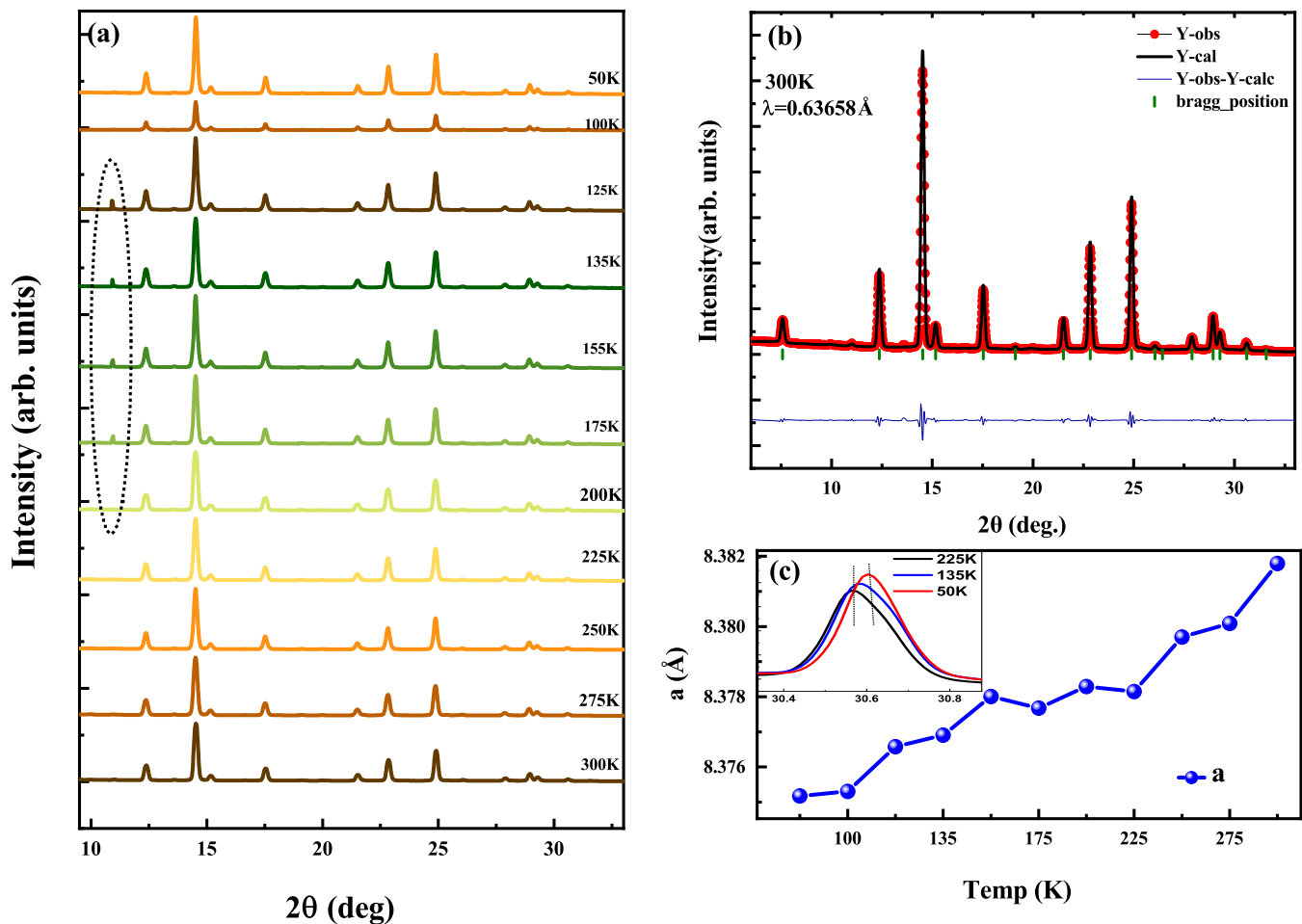


FIG. 2. (a) XRD patterns of CoFe₂O₄ measured in the temperature range of 50–300 K; (b) Rietveld refinement results of the XRD pattern at 300 K; (c) Variation of lattice parameter as a function of temperature with the inset showing the temperature-dependent shift in peak position for selected temperatures (50K, 135K, 225K).

amplified in inverse spinels due to mixed cation occupancy, making Raman spectroscopy sensitive to subtle structural and electronic changes.

Factor group analysis predicts that the ideal spinel structure with space group $Fd-3m$ exhibits five first-order Raman-active modes: $A_{1g} + E_g + 3T_{2g}$. In mixed spinels, a significant increase in Raman-active modes is typically observed due to symmetry lowering caused by structural distortions [11]. The temperature-dependent Raman spectra of CFO reveal distinct phonon shifts which highlight the interplay between lattice dynamics, spin-phonon coupling, and charge redistribution, as shown in Fig. 4. At high temperatures (300–200 K), the $T_{2g}(1)$ mode (Fe³⁺–O bending, octahedral) exhibits slight softening from 196.1 cm⁻¹ to 192.7 cm⁻¹, reflecting thermal expansion. The E_g mode, involving mixed tetrahedral-octahedral vibrations, also softens. The mode at 565.4 cm⁻¹ observed at 300 K begins to soften below 200 K, indicating the onset of changes in magnetic arrangement likely associated with spin-

phonon coupling [12–14]. Additionally, the A_{1g} mode (tetrahedral Fe–O stretching) shifts from 658.3 cm⁻¹ to 665.6 cm⁻¹, likely due to cation redistribution [15–17]. As the temperature further decreases to the 200–100 K range, phonon hardening becomes evident, particularly in the A_{1g} mode (from 690.4 cm⁻¹ to 693.1 cm⁻¹) and $T_{2g}(3)$ (from 614.2 cm⁻¹ to 617.9 cm⁻¹), indicating increased lattice stiffness and enhanced magnetoelastic coupling. The $A_{1g}(2)$ mode also shows unexpected softening around 145 K.

These phonon anomalies are indicative of evolving orbital-lattice interactions and possible local structural rearrangements. In particular, the pronounced softening of the $E_g(2)$ mode and the shift in spin-phonon coupling below 200 K suggest the emergence of short-range orbital correlations and distortions. This behavior is characteristic of JTD, inducing local lattice distortions [1]. Below 100 K, the hardening and stabilization of the A_{1g} and E_g modes indicate that orbital fluctuations have frozen out [3], resulting in a disordered orbital configuration. This is

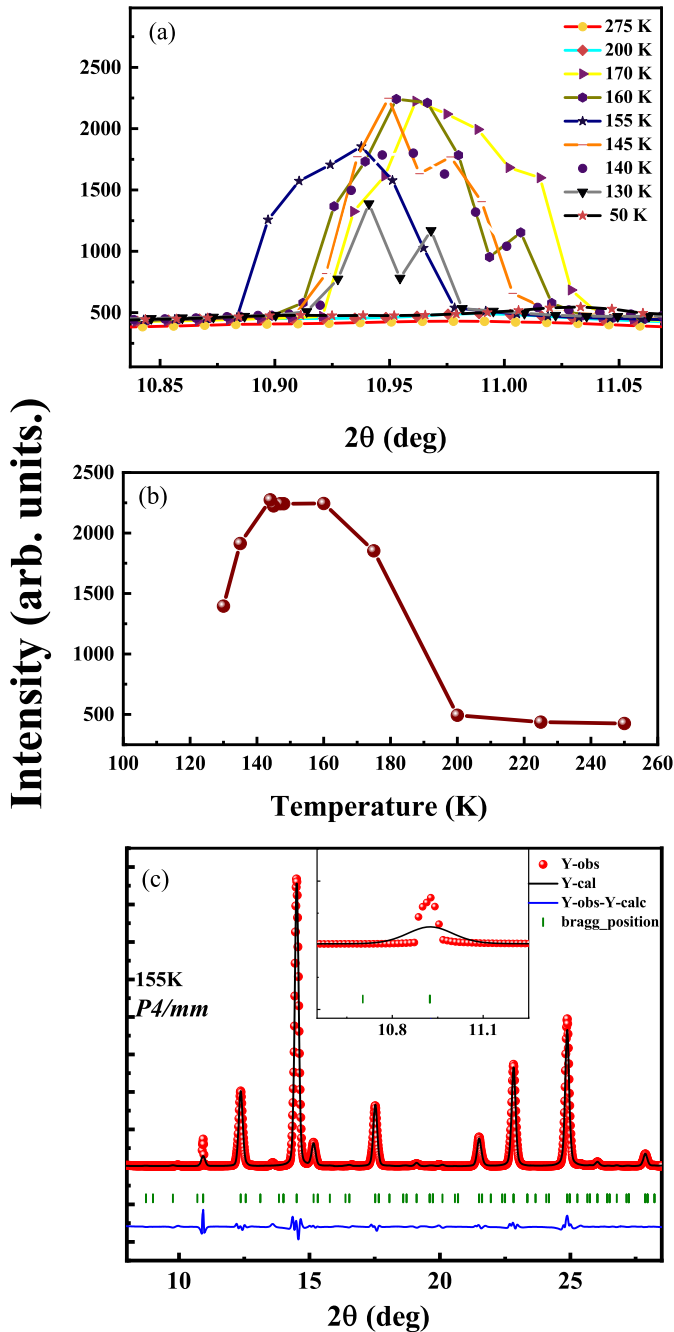


FIG. 3. (a) Temperature evolution of the superlattice peak at $2\theta \approx 10.95^\circ$. (b) Temperature dependence of its intensity. (c) Le Bail fit at 155 K using $P4/mmm$ symmetry; inset shows the superlattice peak and Bragg position.

consistent with a frozen orbital glass state, in which local lattice distortions persist without a macroscopic change in symmetry. The presence of additional Raman modes across all temperatures further suggests persistent structural distortion [11, 12, 18], and cationic disorder, all of which contribute to the complex vibrational behaviour observed in CFO. The influence of magnetic ordering on Raman mode can be evidenced clearly from the magneti-

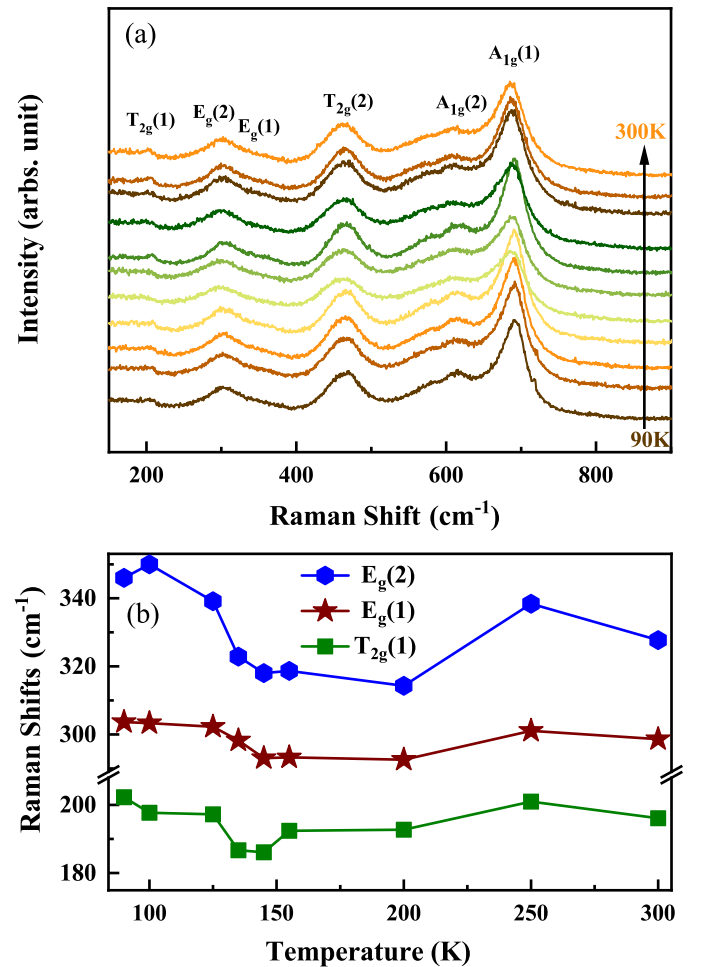


FIG. 4. (a) Raman spectra recorded over the temperature range of 90K to 300K, showing intensity variations with Raman shift. (b) Temperature dependence of Raman shifts for $T_{2g}(1)$, $E_g(1)$, and $E_g(2)$ modes.

sation data described below.

Magnetisation

The temperature-dependent magnetisation curves of CFO (Fig. 5) reveal a clear thermal hysteresis between field-cooled cooling (FCC) and warming (FCW) in the 200–100 K range, indicating a first-order-like transition and also suggesting magnetic metastability and frustration, primarily arising from the interplay of antiferromagnetic and ferromagnetic exchange interactions between tetrahedral (A-site) and octahedral (B-site) cations via oxygen. It should be noted that in this temperature range, we also observed superlattice reflection in XRD, anomaly in lattice parameter, and Raman behaviour. These occurrences indicate towards coupling between spin and degrees of freedom. In this temperature window, JTD at octahedral sites may partially lift orbital

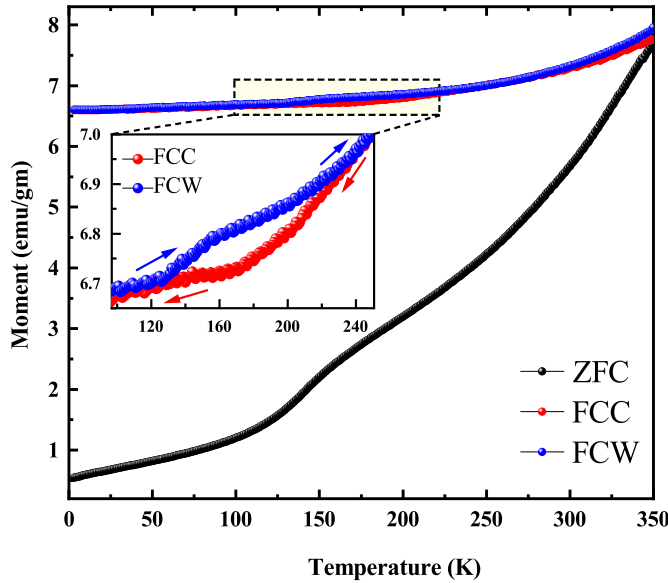


FIG. 5. Magnetization data of CoFe_2O_4 , showing the temperature dependence of magnetization measured under zero-field-cooled (ZFC), field-cooled warming (FCW), and field-cooled cooling (FCC) conditions. The main plot highlights the magnetic behavior and transitions across the temperature range, while the inset illustrates the bifurcation between the FCC and FCW curves.

degeneracy, modulating the magnetic exchange interactions [1]. The resulting spin frustration and orbital-lattice coupling can lead to short-range orbital correlations [1]. These effects are consistent with the Kugel-Khomskii model [8, 19], where orbital occupancy influences magnetic exchange pathways. Similar phenomena have been reported in manganites and vanadates. Below 100 K, the convergence of FCC and FCW curves and the hardening of Raman modes point to a frozen orbital configuration, suggestive of an orbital ordering, with the observed hysteresis linked to fluctuating orbital states [3] and spin reorientation.

The interplay between antiferromagnetic and ferromagnetic interactions becomes more pronounced at temperatures in between 200 K to 100 K. The observed changes suggest a crucial role of A-B superexchange interactions, where $\text{Fe}^{3+}\text{-O-Fe}^{2+}$ and $\text{Co}^{2+}\text{-O-Co}^{3+}$ charge fluctuations influence the overall magnetic structure. This interplay leads to spin frustration effects and local magnetic ordering, which are also reflected in the temperature-dependent Raman shifts and broadening of phonon modes.

Hard X-ray photoemission spectroscopy

To examine the chemical valence states of Co and Fe in CoFe_2O_4 (CFO), the core-level spectra were analysed using X-ray photoelectron spectroscopy (XPS). Figure-

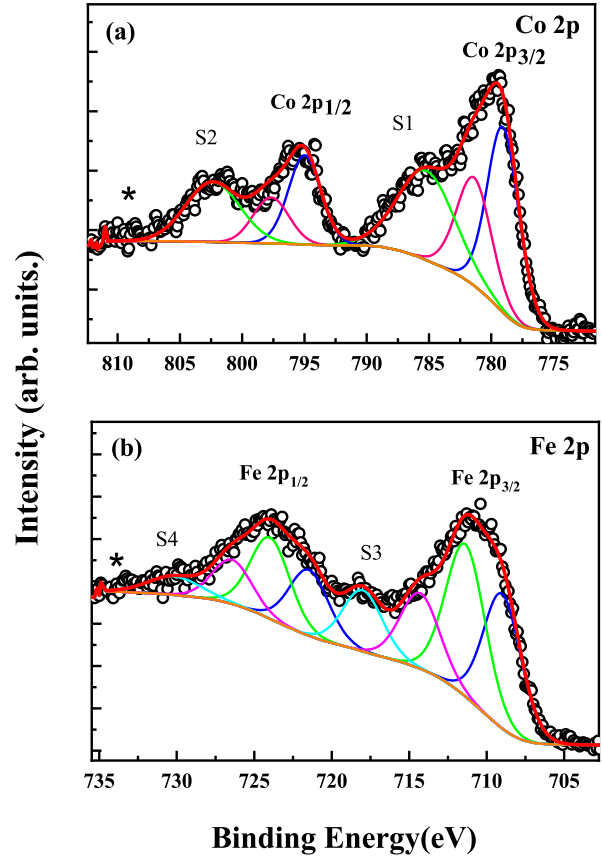


FIG. 6. The 2p core level of (a) Co and (b) Fe excited by 4 keV synchrotron radiation.

6 illustrates the Co and Fe 2p core-level spectra of CFO using 4 keV photon energy. Both Co 2p and Fe 2p spectra are complex and exhibit multiple features as seen. The spectra were numerically deconvoluted using Gaussian and Lorentzian line shape functions. The background was meticulously fitted using the Shirley method, ensuring precise determination of peak positions and relative intensities for a comprehensive analysis. The Co and Fe 2p core-level spectra, split into $2p_{1/2}$ and $2p_{3/2}$ components due to spin-orbit coupling, as indicated in the Fig. 6. The asymmetry and broadening of the spectral features indicate the presence of multiple valence states for both Co and Fe. Considering this asymmetry and broadening, the Co 2p XPS spectrum has been deconvoluted into distinct peaks centered at 779.0 eV ($\text{Co}^{2+} 2p_{3/2}$), 781.3 eV ($\text{Co}^{3+} 2p_{3/2}$), 794.9 eV ($\text{Co}^{2+} 2p_{1/2}$), and 797.6 eV ($\text{Co}^{3+} 2p_{1/2}$). Additionally, two satellite features are observed at 785.20 eV and 802.36 eV, respectively [20, 21]. The presence of Co^{3+} ions in the sample is attributed to cation inversion or Co antisite defects, involving the exchange of Fe and Co ions

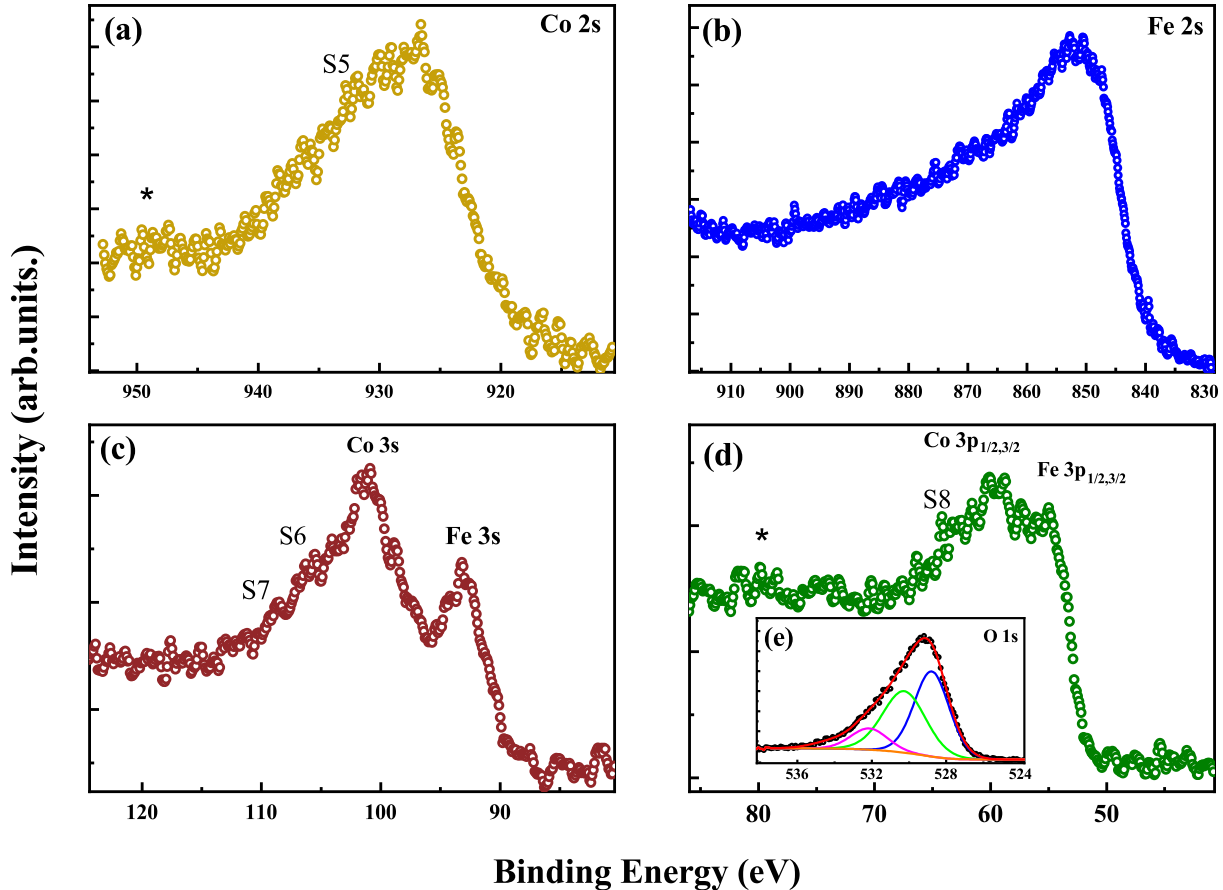


FIG. 7. Core-level spectra excited by 4 keV synchrotron radiation: (a) Co 2s, (b) Fe 2s, (c) Co and Fe 3s, and (d) Co and Fe 3p. The inset in (d) presents the corresponding (e) O 1s spectrum.

between the A and B sites. Specifically, we assume that Co ions occupying the A site exist in the Co^{3+} oxidation state, while Fe ions migrating from the A site to the B site retain their Fe^{3+} state [22].

The Fe 2p XPS spectrum, considering its asymmetry and broadening, has been deconvoluted into distinct peaks at 709 eV ($\text{Fe}^{2+} 2p_{3/2}$), 711.3 eV ($\text{Fe}^{3+} 2p_{3/2}$), 721.4 eV ($\text{Fe}^{2+} 2p_{1/2}$), and 723.9 eV ($\text{Fe}^{3+} 2p_{1/2}$). Additionally, the satellite features have been fitted with four peaks at 714.3 eV, 718.0 eV, 726.4 eV, and 730.1 eV, respectively[23].

The 2s and 3s,3p core-level states of Co and Fe are discussed below. The binding energies of Fe's 3s and 3p levels overlap significantly with those of Co, making it somewhat difficult to clearly describe the satellite features of Fe in these levels. For Co 2s, the main peak appears around 927.3 eV, while the satellite feature, denoted as S5, arises at approximately 932.6 eV. The separation between the main peak and the satellite peak in the Co 2s shell is about 5.3–5.6 eV, which is too large to be ex-

plained by multiplet splitting [21]. Instead, the satellite peak S5 is attributed to an O $2p \rightarrow \text{Co} 3d$ shakeup process. Similarly, the satellite structures (peaks S1 and S2) observed in the Co $2p_{3/2}$ and $2p_{1/2}$ regions are also assigned to the same shakeup process, as they exhibit similarities to peak S5 in the Co 2s region in terms of both intensity and location. The unusually broad widths of the main peak and S5 in the Co 2s spectrum are thought to result from multiplet splitting in addition to Coster-Kronig processes.

In the Co 3s photoemission spectrum, the main peak is observed at 101.2 eV, with two satellite peaks, S6 and S7, appearing at 106.3 eV and 112.3 eV, respectively. The complex structure of the Co 3s peak is primarily due to multiplet splitting, which occurs when different electronic states interact and split into multiple peaks. However, the strong satellite features in the Co 2p and 2s regions suggest that peak S6 is caused by both multiplet splitting and a shakeup process, where an electron is ejected and another electron is excited to a higher energy level.

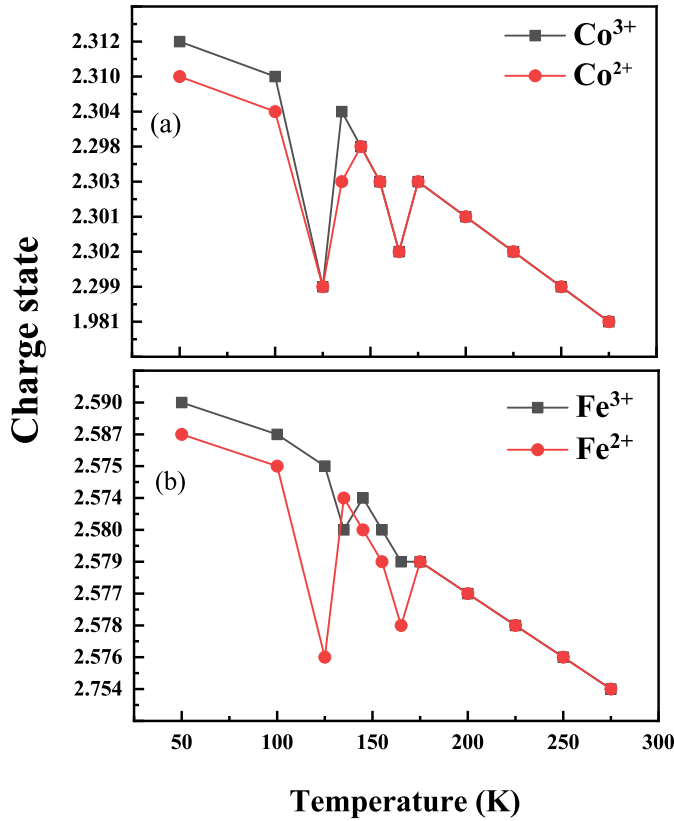


FIG. 8. Temperature-dependent bond valence sum (BVS) of (a) Co and (b) Fe ions in CoFe_2O_4 .

The lower binding-energy side of peak S6 is attributed to multiplet splitting, while the higher binding-energy side is due to shakeup. Peak S7 is related to the shakeup process connected to the multiplet splitting in peak S6. To fully understand the Co 3s spectrum, detailed theoretical calculations are needed to explain the interaction of these effects. In the Co 3p region, the satellite structure is less clearly defined compared to the Co 3s region. The main component of S8 is thought to originate from multiplet splitting. Weak satellite structures, about 20 eV below the main peaks in the Co 2s, 2p, 3s, and 3p regions, are denoted with a symbol (*) and are associated with characteristic energy loss. The observed multiplet splitting energy in Co is $\Delta E_{3s} \sim 5.1$ eV.

In the Fe 2s core-level spectrum, the main peak is observed around 851.7 eV [24]. The region around this peak is broad, but no additional satellites are clearly visible because of low signal-to-noise ratio [25]. The broadening of the main peak may be due to effects such as multiplet splitting or broadening from other electronic interactions, but without clear satellite peaks, the interpretation is less complex compared to the other core levels. In the Fe 3p core-level spectrum, the main peak is observed around 55.9 eV [26]. However, at higher binding energies, the Fe 3p spectrum merges with the Co 3p spectrum, making it

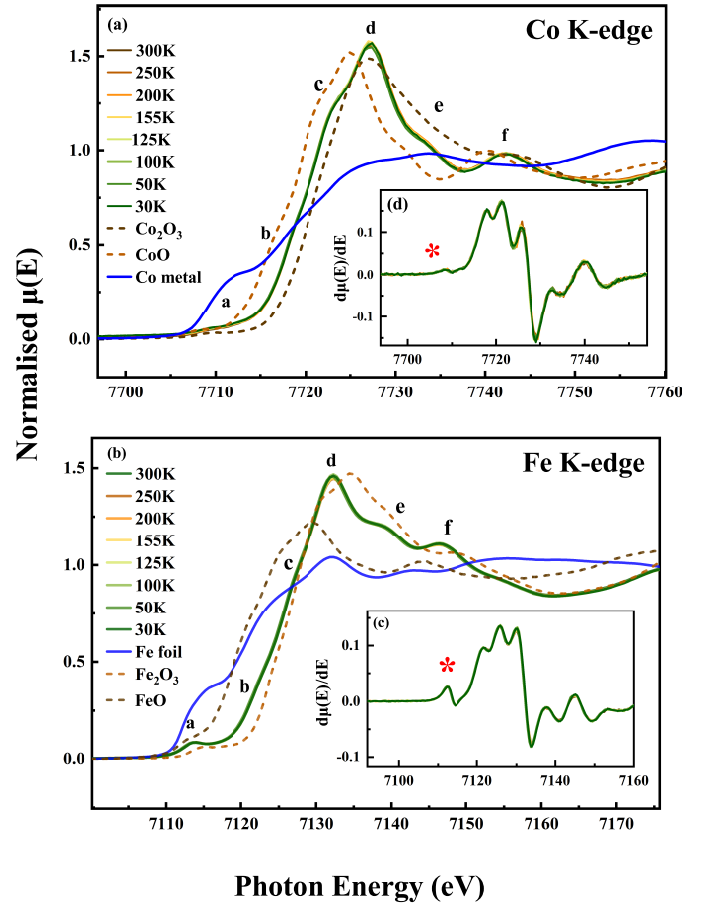


FIG. 9. (a) Normalized XANES spectra of CoFe_2O_4 , highlighting the main absorption region of Co K-edge (b) Normalized Fe K-edge XANES spectra. (c) and (d) display the first derivative of the experimental absorption spectra for the Co K-edge and Fe K-edge, respectively.

difficult to analyze or identify any distinct satellite features for Fe 3p. Similarly, in the Fe 3s spectrum, the main peak appears at approximately 93.5 eV, but its higher binding energy side merges with the Co 3s peak. Due to these overlaps and the merging of spectral features, it is not possible to clearly define or explain the satellite structures in the Fe core-level spectra. Deconvolution of the O 1s XPS spectra in insert Figure 7(d) reveals three main peaks at binding energies of 529.8, 531.5, and 533.3 eV, corresponding to lattice oxygen (O_L), oxygen vacancies or defects (O_V), and chemisorbed oxygen species (O_C), respectively [27].

The chemical valency analysis of the CFO samples, based on the integrated intensities of the fitted XPS peaks, reveals a mixed-valence state for both Co and Fe ions. The results indicate that cobalt is present as approximately 65% Co^{2+} and 35% Co^{3+} , while iron shows a distribution of about 44.7% Fe^{2+} and 55.3% Fe^{3+} .

Again, to evaluate the oxidation states of the Co and Fe cations in CoFe_2O_4 , bond valence sum (BVS) cal-

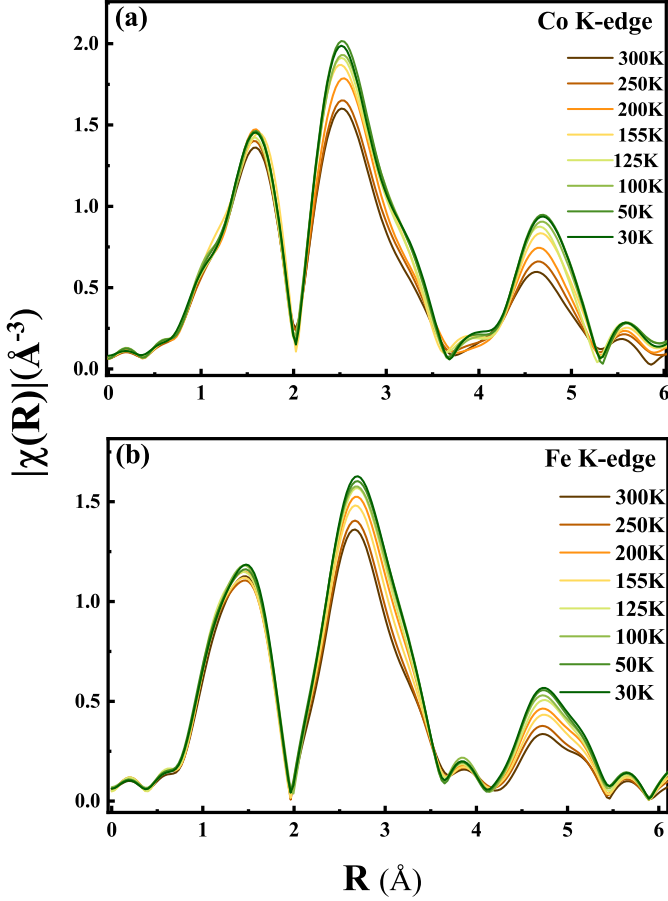


FIG. 10.

The temperature-dependent EXAFS data: (a) Co K-edge, (b) Fe K-edge.

culations were performed using the inbuilt module in the FullProf Suite [10]. The BVS method estimates the valence state V of a cation based on its local bonding environment using the expression $V = \sum_i \exp\left(\frac{d_0 - d_i}{0.37}\right)$, where d_i represents the experimentally determined bond lengths to surrounding anions, and d_0 is a tabulated empirical parameter characteristic of the specific cation-anion pair [28, 29]. Therefore, the local distortion from regular tetrahedral and octahedral (O_h) environment have been investigated by calculating the bond-valence sum (BVS) of Co/Fe-O in Co/FeO₄ tetrahedral and Co/FeO₆ octahedra environment for different temperatures across the structural (across the super-lattice peak) phase transition. We have not observed much change above the super-structure phase transition i.e. 200 K. However, below 200 K, we have found pronounced changes in Co/Fe-O bond distance indicating main role of lattice distortion due to phase-transitions, as is clearly reflected in BVS as a function of temperature, (shown in Fig. 8 (a, b)). These results clearly suggest

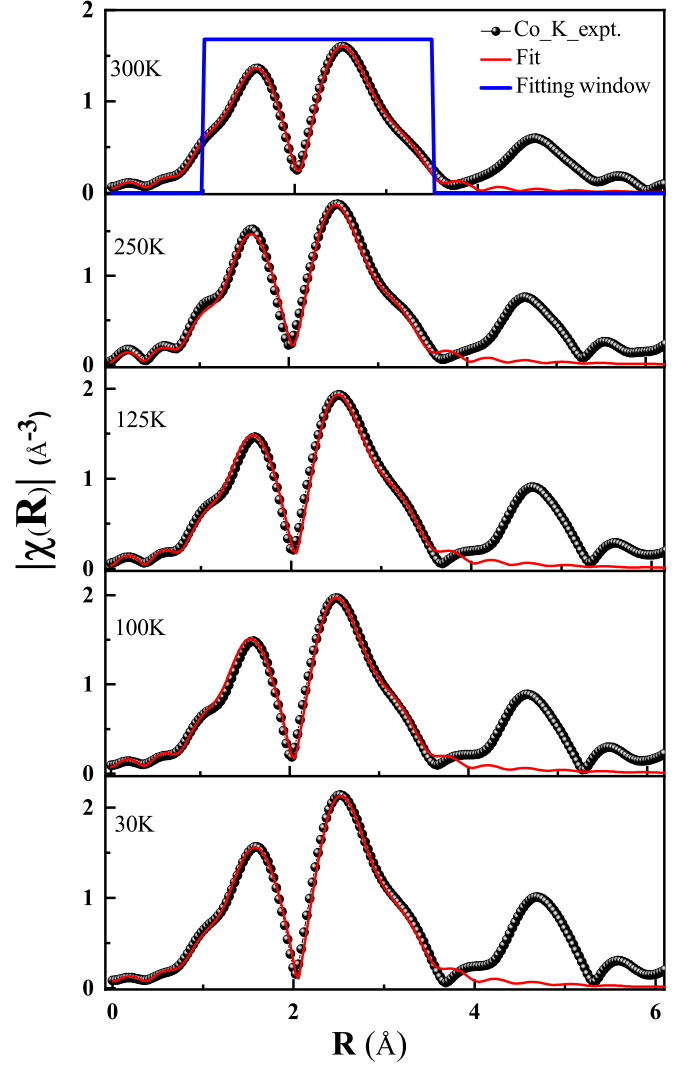


FIG. 11. Fitting of the $|\chi(R)|$ spectra at the Co K-edge in R-space. The modulus of the Fourier transform ($|FT|$) of k^3 -weighted Fe EXAFS data is shown along with the best-fit curves. The data is displayed for a range of temperatures.

that distortion led bond-length variation as a function of temperature across the super-structure phase-transition shows strong lattice-coupling, which leads to symmetry-breaking in CoFe₂O₄. Thus, resulting BVS values exhibit clear temperature-dependent variations in the effective charge states of both Co and Fe. These shifts become more pronounced in the intermediate temperature range ($T_o \approx 200$ – 100 K), suggesting dynamic charge redistribution between Co²⁺/Co³⁺ and Fe²⁺/Fe³⁺. Such fluctuations may reflect short-range charge ordering or charge-orbital correlations [30] shown in Fig. 8, which are consistent with the structural distortions, phonon anomalies, and hysteresis in the temperature-dependent magnetic behavior observed in the same temperature regime.

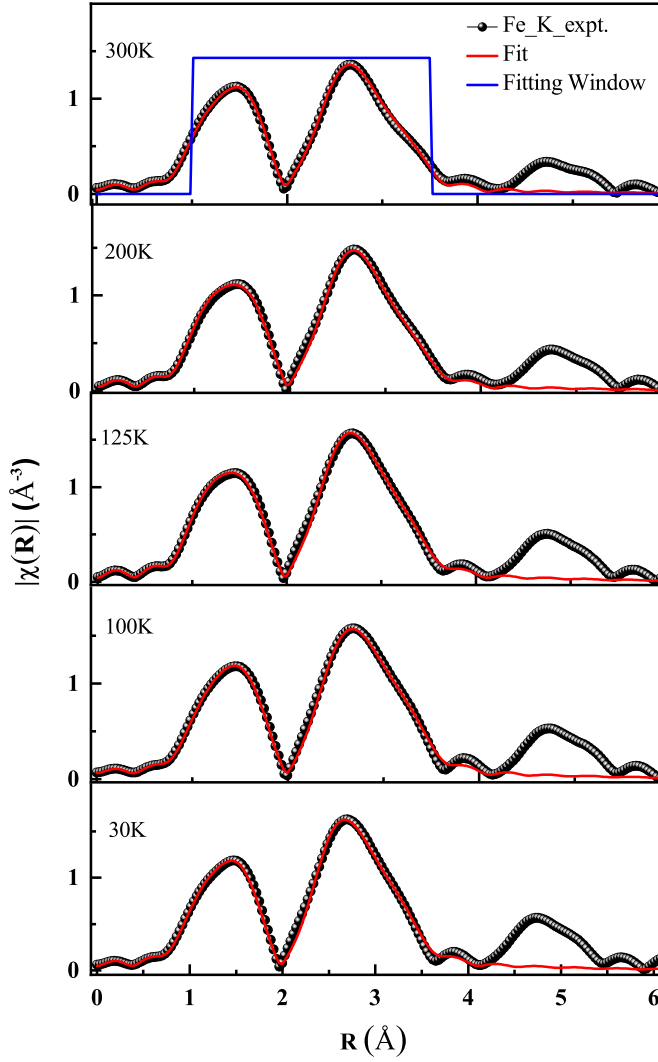


FIG. 12. Fitting of the $|\chi(R)|$ spectra at the Fe K-edge in R-space. The modulus of the Fourier transform ($|FT|$) of k^3 -weighted Fe EXAFS data is shown along with the best-fit curves. The data is displayed for a range of temperatures.

X-ray absorption fine structure spectroscopy

X-ray absorption near edge spectroscopy (XANES)

The XAFS signal provides information about interatomic distances, atomic structure, and the electrical nature of the absorber. It is typically divided into the EXAFS (extended) and XANES (near-edge) regions. The normalized Co and Fe K-edge are presented in Fig.9 to probe the electronic structure around both Fe and Co atoms. The XANES region provides rich structural and electronic information and is generally weakly temperature-dependent due to the Debye-Waller factor ($e^{-2k^2\sigma^2}$) [31, 32]. The edge position reflects the valence state of the photoabsorber. With the extended mean free path of low-energy photoelectrons, multiple scatter-

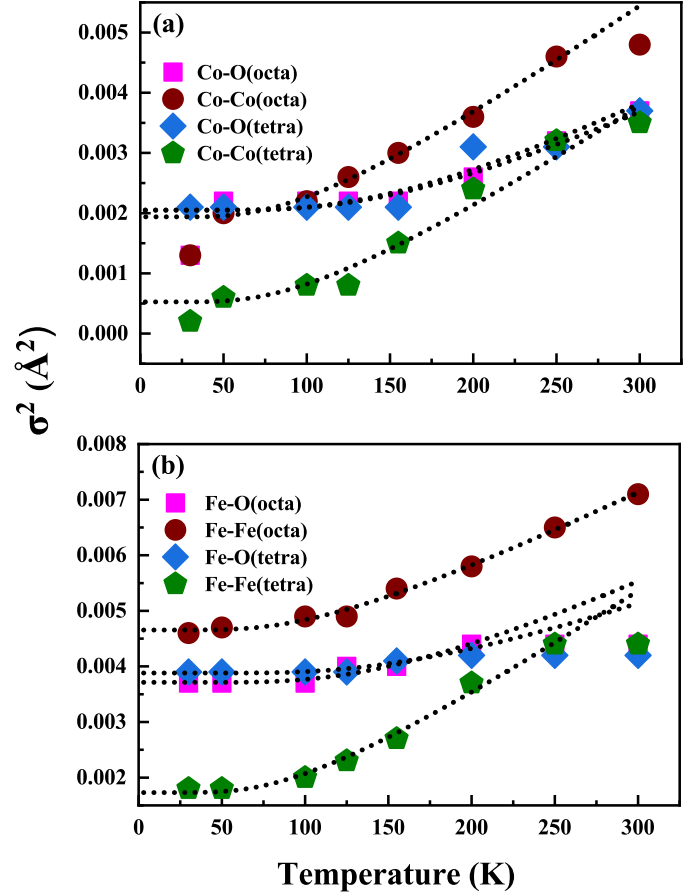


FIG. 13. Debye-Waller factor from EXAFS analysis for CFO samples. The dashed lines are the best-fit data obtained using a correlated Einstein model (a) Co-K edge, (b) Fe-K edge.

ing effects significantly influence the XANES features, making them highly sensitive to the coordination symmetry around the photoabsorber. Additionally, pre-edge analysis offers valuable insights, particularly for the K-edges of 3d metals. The Co and Fe K-edge XANES spectra were processed using standard methods, including pre-edge removal, post-edge atomic background subtraction (α_0), and edge jump normalization [33, 34]. The edge energy (E_0), defining the origin of the photoelectron wave vector $k = \hbar^{-1}\sqrt{2m_e(E - E_0)}$ (m_e being the electron mass), was determined at the midpoint of the edge rise and refined during analysis.

The Co and Fe K-edge XANES spectra show similar behavior with respect to temperature, with the standard deviation between the normalized spectra being less than 10^{-3} . The pre-edge feature is due to electronic transitions from the 1s core level of the absorbing atom (e.g., Co or Fe) to unoccupied d states. The intensity of this pre-edge feature increases with the degree of p-d hybridization [35–37]. Here we note that the low-intensity pre-edge features in the XANES spectra of transition metal oxides arise from 1s electron transitions to un-

occupied d states (quadrupole transitions, $\Delta l = 2$) or to d states hybridized with p states (metal or oxygen 2p) [35, 37, 38]. According to group theory, ideal octahedral symmetry (O_h) prevents p-d mixing, leading to the absence of pre-edge features. However, structural distortions break this symmetry, allowing p-d hybridization and enhancing the pre-edge intensity, which becomes more pronounced with increasing off-center displacement of the absorbing atoms.[35, 37]. For the Co K-edge XANES spectra of CoFe_2O_4 , no significant pre-edge intensity is observed near 7708.40 eV, whereas for Fe, a pre-edge feature is clearly distinct around 7111 eV. This difference indicates a more pronounced pre-edge feature for Fe in the FeO_6 octahedra and the weak pre-edge feature for Co may also result from thermally induced dynamic distortions in the CoO_6 octahedra, observable at both room and low temperatures. The pre-edge feature in both edges is denoted as 'a' in Fig. 9(a, b) and marked with (*) in Fig. 9(c, d). The rising edge (approximately 7717 eV for Co and 7121 eV for Fe) and other distinct features (labeled b, c, d, e, f) in both edge spectra [see Fig. 9 (a,b)] have been analyzed. A shift of approximately 1 eV in the rising edge of the XANES spectra is observed upon cooling, while the white line remains nearly unchanged, indicating no significant change in the oxidation state of Co and Fe. This shift is attributed to Jahn-Teller distortion at low temperature, which leads to elongation of Co/Fe-O bonds. As previously reported,[39, 40] such bond-length variations can induce shift in the edge positions, often exceeding those caused by initial-state effects due to electronic configuration changes, which are typically less than 1 eV. This behaviour is consistent with ligand field theory, wherein back-donation from ligands partially compensates for charge transfer, resulting in minimal changes to the effective charge on the metal ions[39, 40]. Comparisons with reference samples, such as Co_3O_4 and CoO for Co, and FeO and Fe_2O_3 for Fe, confirm the mixed valence state of Co and Fe across all temperature ranges.

The minor feature labeled 'b', observed around 7717 eV and 7121 eV, respectively (shown in fig-9 (a,b)) for Co and Fe-edge, respectively, is attributed to charge transfer from oxygen to Co or Fe ions in the final state, which results from the strong hybridization between Co or Fe 3d and O 2p orbitals. This suggests a small charge transfer energy in these compounds. The white line for both Co and Fe K-edges is observed around 7725 eV and 7126 eV, respectively, and is primarily attributed to the $1s \rightarrow 4p$ dipole transition. The position of the white line is influenced by both the valence state and the local coordination of the absorbing atom [41]. Octahedral site disorder affects the main-edge feature similarly for both Co and Fe K-edge spectra, indicating that the white line intensity is mainly controlled by the level of octahedral distortion. In the temperature range associated with orbital ordering, no noticeable change was observed in the white line in-

tensity. The post-edge features (E, F) observed in the Co and Fe K-edge XANES spectra of CoFe_2O_4 correspond to electronic transitions in which 1s electrons from Co or Fe are excited into Co 4p or Fe 4p states. These 4p states are strongly hybridized with O 2p orbitals, reflecting the interaction between cobalt, iron, and oxygen in the lattice.

The linear combination fit (LCF) analysis of the XANES of the reference file yielded consistent results with the HXPES data. For cobalt, the analysis indicated that the sample contains approximately 65% Co^{2+} and 35% Co^{3+} , while for iron, it revealed a distribution of around 45% Fe^{2+} and 55% Fe^{3+} at room temperature. This analysis suggests that a fraction of the Co^{2+} ions may have migrated to the A site and oxidized to Co^{3+} , while a portion of the Fe^{3+} ions are originally at the A site shifted to the B site and reduced to Fe^{2+} , preserving charge neutrality. This implies the formation of antisite defects, where Co ions move from the B site to the A site, while Fe ions at the A site relocate to the B site [22].

Extended X-ray absorption fine structure (EXAFS)

Before discussing the results of EXAFS, it is important to highlight the complementary nature of XAFS and XRD techniques. XRD captures structural features with periodic repetition in unit cells, while non-periodic features contribute only to a diffuse background. In contrast, XAFS focuses on the local structure around the absorber, regardless of short- or long-range order. This distinction highlights the unique and complementary insights provided by the two methods [31]. Generally, non-periodic features in the atomic distribution can cause the interatomic distances obtained from EXAFS analysis to differ significantly from those between atomic sites in the periodic lattice.

In the EXAFS region, the signal is dominated by single photoelectron scattering (SS) and selected multiple scattering (MS) processes from nearly collinear atomic configurations, with enhancements from forward scattering effects [42, 43]. The EXAFS signal is typically modeled using the standard EXAFS formula, which describes the average local structure around the absorber as a sum of Gaussian-shaped interatomic shells. Each shell is characterized by its multiplicity (N), average distance (R), and mean square relative displacement (MSRD, σ^2) [43]. The σ^2 consists of a temperature-dependent component, which accounts for thermally activated lattice vibrations, and a temperature-independent static component:

$$\sigma^2 = \sigma_E^2(T) + \sigma_{\text{static}}^2. \quad (1)$$

The temperature-dependent term is accurately described

by a correlated Einstein model [44].

$$\sigma_E^2(T) = \frac{\hbar}{\mu\omega_E} \coth\left(\frac{\hbar\omega_E}{2k_B T}\right). \quad (2)$$

Note that at low temperatures (T less than approximately 60–70 K), $\sigma_E^2(T)$ typically remains nearly constant [42, 43]. By ensuring the stability and reproducibility of the experimental setup and minimizing correlations between fitting parameters (e.g., by fixing ΔE and coordination numbers), the accuracy in determining relative variations in structural parameters as a function of external factors like temperature can be improved significantly, as demonstrated in studies of thermal expansion in solids [44]. While analyzing next-neighbor shells, accuracy may decrease due to signal overlap, parameter correlations, and the need to merge or neglect certain contributions. However, the relative variations in parameters can reveal even subtle structural effects.

Fig. 10 shows the temperature-dependent EXAFS data at the (a) Co K-edge and (b) Fe K-edge. The y -axis represents the magnitude of the Fourier-transformed EXAFS function, $|\chi(R)|$ (in \AA^{-3}), while the x -axis shows the radial distance R (in \AA) from the absorbing atom, corresponding to the real-space positions of neighboring atoms, revealing an increase in local structural disorder with rising temperature. At both edges, the amplitudes of the $\chi(R)$ peaks decrease with temperature in both coordination shells, indicating thermal vibrations.

Figures 11 and 12 show the fitting of temperature-dependent EXAFS data for both Co and Fe edges across all temperatures. The corresponding fitting parameters are provided in Tables 1 and 2. The findings from the fitting analysis are summarised below. The results highlight key temperature-dependent trends in local structural parameters, particularly in the Co–O and Fe–O bond lengths. At higher temperatures (above 155 K), the Co–O and Fe–O bond lengths in octahedral coordination remain nearly uniform, consistent with an undistorted local environment. However, a clear bond length splitting is observed at or below 155 K, 125 K, and 100 K for both Co–O and Fe–O octahedral paths. This behaviour is a hallmark of Jahn–Teller distortion (JTD), [8] in octahedrally coordinated Co^{2+} and Fe^{3+} ions [Fig. 1] and leads to anisotropic elongation of the surrounding oxygen bonds which modify the spin ground state of Co^{2+} and Fe^{3+} ions due to crystal electric field (CEF) [Fig. 1]. This separation vanishes again at lower temperatures (50 K and 30 K), where the bond lengths return to near uniform values, suggesting a suppression or freezing of dynamic distortions. In addition, from the temperature dependent SR-XRD along with EXAFS as a local probe measurements, we have observed evidence of superstructure, which occurs due to significant local distortion of $\text{CoO}_4/\text{FeO}_4$ and $\text{CoO}_6/\text{FeO}_6$ at structural transition ($T_o = 200$ K), strongly influencing the spins associated

T (K)	Path	N	R (\AA)	σ^2 (\AA^2)
300K	Co-O (Octa)	6	2.103 ± 0.002	0.0037 ± 0.0002
	Co-Co (Octa)	6	3.008 ± 0.003	0.0048 ± 0.0001
	Co-O (Tetra)	4	1.916 ± 0.002	0.0037 ± 0.0003
	Co-Co (Tetra)	4	3.491 ± 0.003	0.0035 ± 0.0003
250K	Co-O (Octa)	6	2.103 ± 0.002	0.0032 ± 0.0002
	Co-Co (Octa)	6	3.008 ± 0.003	0.0046 ± 0.0003
	Co-O (Tetra)	4	1.919 ± 0.002	0.0031 ± 0.0003
	Co-Co (Tetra)	4	3.491 ± 0.003	0.0032 ± 0.0003
200K	Co-O (Octa)	6	2.103 ± 0.002	0.0026 ± 0.0002
	Co-Co (Octa)	6	3.008 ± 0.003	0.0036 ± 0.0003
	Co-O (Tetra)	4	1.919 ± 0.002	0.0031 ± 0.0003
	Co-Co (Tetra)	4	3.491 ± 0.003	0.0024 ± 0.0003
155K	Co-O1 (Octa)	4	2.078 ± 0.002	0.0022 ± 0.0002
	Co-O2 (Octa)	2	2.41 ± 0.002	0.0022 ± 0.0002
	Co-Co (Octa)	6	3.008 ± 0.003	0.0030 ± 0.0003
	Co-O (Tetra)	4	1.919 ± 0.002	0.0021 ± 0.0003
	Co-Co (Tetra)	4	3.491 ± 0.003	0.0015 ± 0.0003
125K	Co-O1 (Octa)	4	2.084 ± 0.002	0.0022 ± 0.0002
	Co-O2 (Octa)	2	2.126 ± 0.002	0.0022 ± 0.0002
	Co-Co (Octa)	6	3.008 ± 0.003	0.0026 ± 0.0003
	Co-O (Tetra)	4	1.919 ± 0.002	0.0021 ± 0.0003
	Co-Co (Tetra)	4	3.491 ± 0.003	0.0008 ± 0.0003
100K	Co-O1 (Octa)	4	2.092 ± 0.002	0.0022 ± 0.0002
	Co-O2 (Octa)	2	2.132 ± 0.002	0.0022 ± 0.0002
	Co-Co (Octa)	6	3.008 ± 0.003	0.0022 ± 0.0003
	Co-O (Tetra)	4	1.919 ± 0.002	0.0021 ± 0.0003
	Co-Co (Tetra)	4	3.491 ± 0.003	0.0008 ± 0.0003
50K	Co-O (Octa)	6	2.103 ± 0.002	0.0022 ± 0.0002
	Co-Co (Octa)	6	3.008 ± 0.003	0.0020 ± 0.0003
	Co-O (Tetra)	4	1.919 ± 0.002	0.0021 ± 0.0003
	Co-Co (Tetra)	4	3.491 ± 0.003	0.0006 ± 0.0003
30K	Co-O (Octa)	6	2.103 ± 0.002	0.0013 ± 0.0002
	Co-Co (Octa)	6	3.008 ± 0.003	0.0013 ± 0.0003
	Co-O (Tetra)	4	1.919 ± 0.002	0.0021 ± 0.0003
	Co-Co (Tetra)	4	3.491 ± 0.003	0.0002 ± 0.0003

TABLE I. Co K-edge EXAFS data fitting, where CN (coordination number) was kept as a fixed parameter, and R (bond distance) and σ^2 (Debye-Waller factor) were variable parameters. The numbers in parentheses indicate the uncertainty in the last digit.

with Co^{2+} and Fe^{3+} . The consequence of this structural transition is orbital correlation transition in CFO. Importantly, significant change in the bond length is not observed in the tetrahedral coordination shells, indicating that the Jahn–Teller distortion is confined to the octahedral sublattice [please see, Fig. 1]. The emergence of JTD in the intermediate temperature range points to a local structural instability, possibly induced by short-range orbital [1, 8] ordering or spin–orbital coupling.

The temperature dependence of the Debye-Waller factor (σ^2) provides critical insights into the local structural dynamics and the extent of disorder within the studied

T (K)	Path	N	R (Å)	σ^2 (Å ²)
300K	Fe-O (Octa)	6	1.998 ± 0.003	0.0044 ± 0.0001
	Fe-Fe (Octa)	6	3.038 ± 0.003	0.0071 ± 0.0001
	Fe-O (Tetra)	4	1.839 ± 0.003	0.0042 ± 0.0001
	Fe-Fe (Tetra)	4	3.523 ± 0.003	0.0044 ± 0.0001
250K	Fe-O (Octa)	6	1.998 ± 0.003	0.0044 ± 0.0001
	Fe-Fe (Octa)	6	3.038 ± 0.003	0.0065 ± 0.0001
	Fe-O (Tetra)	4	1.839 ± 0.003	0.0042 ± 0.0001
	Fe-Fe (Tetra)	4	3.523 ± 0.003	0.0044 ± 0.0001
200K	Fe-O (Octa)	6	1.998 ± 0.003	0.0044 ± 0.0001
	Fe-Fe (Octa)	6	3.038 ± 0.003	0.0058 ± 0.0001
	Fe-O (Tetra)	4	1.839 ± 0.003	0.0042 ± 0.0001
	Fe-Fe (Tetra)	4	3.523 ± 0.003	0.0037 ± 0.0001
155K	Fe-O (Octa)	4	1.998 ± 0.003	0.0040 ± 0.0001
	Fe-O (Octa)	2	2.005 ± 0.003	0.0040 ± 0.0001
	Fe-Fe (Octa)	6	3.038 ± 0.003	0.0054 ± 0.0001
	Fe-O (Tetra)	4	1.839 ± 0.003	0.0041 ± 0.0001
125K	Fe-Fe (Tetra)	4	3.523 ± 0.003	0.0027 ± 0.0001
	Fe-O1 (Octa)	4	1.998 ± 0.003	0.0040 ± 0.0001
	Fe-O2 (Octa)	2	2.005 ± 0.003	0.0040 ± 0.0001
	Fe-Fe (Octa)	6	3.038 ± 0.003	0.0049 ± 0.0001
100K	Fe-O (Tetra)	4	1.839 ± 0.003	0.0039 ± 0.0001
	Fe-Fe (Tetra)	4	3.523 ± 0.003	0.0023 ± 0.0001
	Fe-O1 (Octa)	4	1.999 ± 0.003	0.0039 ± 0.0001
	Fe-O2 (Octa)	2	2.004 ± 0.003	0.0038 ± 0.0001
50K	Fe-Fe (Octa)	6	3.038 ± 0.003	0.0049 ± 0.0001
	Fe-O (Tetra)	4	1.839 ± 0.003	0.0039 ± 0.0001
	Fe-Fe (Tetra)	4	3.523 ± 0.003	0.0018 ± 0.0001
	Fe-O (Octa)	6	1.998 ± 0.003	0.0037 ± 0.0001
30K	Fe-Fe (Octa)	6	3.038 ± 0.003	0.0047 ± 0.0001
	Fe-O (Tetra)	4	1.839 ± 0.003	0.0039 ± 0.0001
	Fe-Fe (Tetra)	4	3.523 ± 0.003	0.0018 ± 0.0001
	Fe-O (Octa)	6	1.998 ± 0.003	0.0037 ± 0.0001
30K	Fe-Fe (Octa)	6	3.038 ± 0.003	0.0046 ± 0.0001
	Fe-O (Tetra)	4	1.839 ± 0.003	0.0039 ± 0.0001
	Fe-Fe (Tetra)	4	3.523 ± 0.003	0.0018 ± 0.0001

TABLE II. Fe K-edge EXAFS data fitting, where CN (coordination number) was kept as a fixed parameter, and R (bond distance) and σ^2 (Debye-Waller factor) were variable parameters. The numbers in parentheses indicate the uncertainty in the last digit.

sample. In the present work, the σ^2 values for Fe-O and Fe-Fe bonds in octahedral coordination exhibit a notable increase with temperature, highlighting the contributions of both thermal vibrations and static disorder. The presence of oxygen vacancies contributes to enhanced lattice instability, as reflected in the progressive rise of σ^2 . For the tetrahedral coordination sites, the σ^2 values of Fe-O and Fe-Fe bonds remain relatively constant and lower compared to the octahedral coordination sites. This indicates that the tetrahedral framework is more resistant to disorder and less impacted by the redistribution of cations or the introduction of oxygen vacancies. Such

structural robustness suggests a localized decoupling between the dynamic behavior of tetrahedral and octahedral sites, with the latter being more susceptible to distortions. The octahedral σ^2 values, particularly for Co-O and Co-Co bonds, exhibit a pronounced temperature-dependent rise, underscoring the pivotal role of cation redistribution and oxygen deficiency in generating disorder. This distinction between octahedral and tetrahedral behavior reflects the asymmetric distribution of strain and local lattice distortions in the sample, primarily concentrated in the octahedral sublattice. The rapid increase in σ^2 for Fe-Fe and Co-Co octahedral bonds highlights the impact of these defects on the structural integrity of the material.

From a broader perspective, the differences in the behavior of σ^2 between tetrahedral and octahedral sites have significant implications for the material's electronic and magnetic properties. The increased disorder in octahedral sites may lead to localized changes in the electronic structure, such as alterations in the crystal field splitting energy, which in turn can influence the orbital occupancy and electronic transitions of Fe and Co ions. These distortions can also affect the magnetic exchange [19] interactions, potentially introducing frustration or disorder into the magnetic ground state.

TABLE III. Fitted Parameters: Einstein Temperature (θ_E) and Static Disorder (σ_S^2)

Bond Type	θ_E (K)	σ_S^2 (Å ²)
Fe-Fe (octa)	337.16 ± 4.07	$2.08 \times 10^{-4} \pm 6.64 \times 10^{-5}$
Fe-Fe (tetra)	291.21 ± 4.67	$1.24 \times 10^{-4} \pm 1.01 \times 10^{-5}$
Fe-O (octa)	650.91 ± 49.68	$8.34 \times 10^{-4} \pm 2.96 \times 10^{-5}$
Fe-O (tetra)	605.63 ± 23.08	$6.71 \times 10^{-4} \pm 1.39 \times 10^{-5}$
Co-O (octa)	496.17 ± 27.24	$1.98 \times 10^{-4} \pm 3.31 \times 10^{-5}$
Co-O (tetra)	510.45 ± 20.40	$1.72 \times 10^{-4} \pm 2.29 \times 10^{-5}$
Co-Co (octa)	289.64 ± 3.64	$9.12 \times 10^{-4} \pm 8.06 \times 10^{-5}$
Co-Co (tetra)	296.30 ± 13.08	$2.29 \times 10^{-4} \pm 3.34 \times 10^{-5}$

Using the Einstein model from Eq. (2), we fitted the Debye-Waller factor, and the results are presented in Fig. 13 for each coordination environment. We observe Fe-Fe octa site shown in Fig. 13(b), the highest disorder. The primary cause of disorder at the Fe sites may be attributed to crystal field splitting (Δ_{CFS}), which significantly influences Fe-Fe interactions, particularly in octahedral environments. In octahedral coordination, Fe³⁺ (d^5) and Fe²⁺ (d^6) ions experience stronger crystal field splitting (Δ_{oct}), which weakens direct Fe-Fe interactions. This reduced interaction strength results in increased flexibility of the Fe sites, making them more susceptible to local structural disorder. In contrast, Fe-Fe interactions within tetrahedral coordination environments experience a much lower crystal field splitting ($\Delta_{\text{tet}} < \Delta_{\text{oct}}$), leading to comparatively greater structural stability. A similar trend is observed for Co sites; however, due to the

weaker Co–O covalency relative to Fe–O, the octahedral Co–Co disorder is less pronounced than that observed in the Fe–Fe (octahedral) network.

CONCLUSION

The structural and electronic disorder in CoFe_2O_4 (CFO), revealed through synchrotron XRD, EXAFS, and XANES, has a pronounced influence on the spectral characteristics observed in HAXPES. Cation redistribution and oxygen vacancies contribute to lattice disorder and local strain within the coordination environment. These effects manifest in HAXPES as broadened and asymmetric Co and Fe core-level spectra, indicative of mixed valence states. The presence of strong shake-up satellite features reflects enhanced charge-transfer excitations and electronic correlations arising from the disordered local structure.

Temperature-dependent EXAFS analysis, through the Debye–Waller factor, confirms an increase in thermal and static disorder, which further impacts the spectral line shapes and multiplet splitting observed in HAXPES. The disruption of local crystal field environments by oxygen vacancies modifies screening conditions and charge-transfer states, highlighting the close coupling between structural distortions and electronic behavior. These findings are reinforced by Raman spectroscopy, which reveals significant temperature-dependent shifts and broadening of A_{1g} , E_g , and T_{2g} modes. The activation of additional Raman modes at lower temperatures, along with phonon anomalies, points to magnetoelastic coupling and dynamic lattice effects.

Magnetic measurements exhibit a clear thermal hysteresis between field-cooled cooling (FCC) and warming (FCW) curves, suggesting competition between tetrahedral and octahedral magnetic sublattices. As temperature decreases, antiferromagnetic and ferromagnetic interactions become increasingly competitive, modifying the local magnetic environment. These changes are reflected in the Raman spectral response, underscoring the strong interplay between lattice, spin, and electronic degrees of freedom.

In conclusion, the detailed temperature dependent structural investigation using powder synchrotron x-ray diffraction and extracted refinement parameters such as unit-cell parameters and bond-lengths as a function of temperature suggests presence of strong distortion, further confirmed from local probe EXAFS. Accordingly, strong lattice-coupling gradually develops orbital correlations in CoFe_2O_4 . These correlations become significant below 200 K, where an emergence of super-lattice peak could remarkably induce symmetry-breaking. This is because of local octahedral and tetrahedral environment distortion, most likely responsible for the origin of orbital order formation in CFO. Around the orbital tran-

sition temperature ($T_o \approx 200\text{--}100$ K), we observe clear signatures of orbital ordering associated with cooperative Jahn–Teller distortions, spin reorientation or evolving exchange interactions, and charge redistribution, as supported by bond valence sum (BVS) analysis. Below T_o , all associated structural, magnetic, and vibrational anomalies vanish, indicating the onset of a frozen, disordered orbital configuration consistent with an orbital glass state. These findings offer new insights into the frustrated coupling of orbital, charge, spin, and lattice sectors in spinel ferrites.

ACKNOWLEDGMENTS

The authors express their sincere gratitude to M.P. Saravanan and the cryogenics team for their assistance in supplying cryogens. We acknowledge the University Grants Commission (UGC), Government of India, for the financial support through a fellowship grant. The authors also thank Pragati Sharma for performing the Raman measurements. Special thanks are due to Priyanshi Tiwari, Rajeev Joshi, Pramod R. Nadig, and Ananya Sahoo or their insightful discussions and valuable suggestions.

* venkatamedicherla@soa.ac.in

† ram@csr.res.in

- [1] Yoshinori Tokura and Naoto Nagaosa. Orbital physics in transition-metal oxides. *science*, 288(5465):462–468, 2000.
- [2] Xin Li, Xiaohua Ma, Dong Su, Lei Liu, Robin Chisnell, Shyue Ping Ong, Hailong Chen, Alexandra Toumar, Juan-Carlos Idrobo, Yuechuan Lei, et al. Direct visualization of the jahn–teller effect coupled to na ordering in na 5/8 mno 2. *Nature materials*, 13(6):586–592, 2014.
- [3] James CT Lee, Shi Yuan, Siddhartha Lal, Young Il Joe, Yu Gan, Serban Smadici, Ken Finkelstein, Yejun Feng, Andrivo Rusydi, Paul M Goldbart, et al. Two-stage orbital order and dynamical spin frustration in kcu3. *Nature Physics*, 8(1):63–66, 2012.
- [4] Mahrous R Ahmed and GA Gehring. Volume collapse in lamno 3 studied using an anisotropic potts model. *Physical Review B—Condensed Matter and Materials Physics*, 79(17):174106, 2009.
- [5] A Trokiner, S Verkhovskii, A Gerashenko, Z Volkova, O Anikeenok, K Mikhalev, M Eremin, and L Pinsard-Gaudart. Melting of the orbital order in lamno 3 probed by nmr. *Physical Review B—Condensed Matter and Materials Physics*, 87(12):125142, 2013.
- [6] Tapan Chatterji, François Fauth, Bachir Ouladdiaf, P Mandal, and B Ghosh. Volume collapse in lamno 3 caused by an orbital order-disorder transition. *Physical Review B*, 68(5):052406, 2003.
- [7] Sen Yang, Xiaobing Ren, and Xiaoping Song. Evidence for first-order nature of the ferromagnetic transition in

- ni, fe, co, and cofe_2o_4 . Phys. Rev. B, 78:174427, Nov 2008.
- [8] R Koborinai, Sachith E Dissanayake, M Reehuis, Masaaki Matsuda, T Kajita, H Kuwahara, S-H Lee, and T Katsufuji. Orbital glass state of the nearly metallic spinel cobalt vanadate. Physical Review Letters, 116(3):037201, 2016.
- [9] K Klementiev and Roman Chernikov. Xafsmass: a program for calculating the optimal mass of xafs samples. In Journal of Physics: Conference Series, volume 712, page 012008. IOP Publishing, 2016.
- [10] Juan Rodríguez-Carvajal. Recent advances in magnetic structure determination by neutron powder diffraction. Physica B: Condensed Matter, 192(1-2):55–69, 1993.
- [11] Tahani Saad Almutairi. Unveiling the impact of spin and cation dynamics on raman spectroscopy in co-ferrite. ACS Physical Chemistry Au, 2024.
- [12] Tahani Saad Almutairi. Unraveling the complex interplay of phase transitions in spinel ferrites: a comprehensive quantum mechanical vibrational study of znfe_2o_4 . ACS omega, 8(40):36999–37010, 2023.
- [13] Jiasi Xu, Jung H Park, and Hyun M Jang. Orbital-spin-phonon coupling in jahn-teller-distorted lamno_3 : Softening of the 490 and 610 cm^{-1} raman-active modes. Physical Review B—Condensed Matter and Materials Physics, 75(1):012409, 2007.
- [14] Qi-C Sun, Christina S Birkel, Jinbo Cao, Wolfgang Tremel, and Janice L Musfeldt. Spectroscopic signature of the superparamagnetic transition and surface spin disorder in cofe_2o_4 nanoparticles. ACS nano, 6(6):4876–4883, 2012.
- [15] Raghvendra Singh Yadav, Ivo Kuřitka, Jarmila Vilcakova, Jaromir Havlica, Jiri Masilko, Lukas Kalina, Jakub Tkacz, Jiří Švec, Vojtěch Enev, and Miroslava Hajdúchová. Impact of grain size and structural changes on magnetic, dielectric, electrical, impedance and modulus spectroscopic characteristics of cofe_2o_4 nanoparticles synthesized by honey mediated sol-gel combustion method. Advances in Natural Sciences: Nanoscience and Nanotechnology, 8(4):045002, 2017.
- [16] P Suchismita Behera, Dharendra Kumar, VG Sathe, and PA Bhohe. Influence of local structural distortions on magnetism and spin-phonon coupling of multiferroic spinel chalcogenide. Journal of Applied Physics, 121(24), 2017.
- [17] P Chandramohan, MP Srinivasan, S Velmurugan, and SV Narasimhan. Cation distribution and particle size effect on raman spectrum of cofe_2o_4 . Journal of Solid State Chemistry, 184(1):89–96, 2011.
- [18] Brajesh Nandan, MC Bhatnagar, and Subhash C Kashyap. Cation distribution in nanocrystalline cobalt substituted nickel ferrites: X-ray diffraction and raman spectroscopic investigations. Journal of Physics and Chemistry of Solids, 129:298–306, 2019.
- [19] Kliment I Kugel and Daniel I Khomskii. Crystal-structure and magnetic properties of substances with orbital degeneracy. Zh. Eksp. Teor. Fiz., 64:1429–1439, 1973.
- [20] Subho Saha, Anita Bagri, Sourav Chowdhury, Priyanka Yadav, and Ram Janay Choudhary. Electronic comprehension of exchange bias effect in $\text{sr}_2\text{coruo}_6$ - δ thin-film. Journal of Applied Physics, 134(18), 2023.
- [21] KS Kim. X-ray-photoelectron spectroscopic studies of the electronic structure of coo . Physical Review B, 11(6):2177, 1975.
- [22] Masaki Kobayashi, Munetoshi Seki, Masahiro Suzuki, Ryo Okano, Miho Kitamura, Koji Horiba, Hiroshi Kumigashira, Atsushi Fujimori, Masaaki Tanaka, and Hitoshi Tabata. Intervalence charge transfer and charge transport in the spinel ferrite ferromagnetic semiconductor $\text{ru-doped co fe}_2\text{o}_4$. Physical Review B, 105(20):205103, 2022.
- [23] Paul S Bagus, Connie J Nelin, Christopher R Brundle, B Vincent Crist, Nabajit Lahiri, and Kevin M Rosso. Combined multiplet theory and experiment for the $\text{fe } 2p$ and $3p$ xps of feo and fe_2o_3 . The Journal of Chemical Physics, 154(9), 2021.
- [24] S Kučas, P Drabužinskis, A Kynienė, Š Masys, and V Jonauskas. Evolution of radiative and auger cascades following $2s$ vacancy creation in fe^{2+} . Journal of Physics B: Atomic, Molecular and Optical Physics, 52(22):225001, 2019.
- [25] KS Kim. Charge transfer transition accompanying x-ray photoionization in transition-metal compounds. Journal of Electron Spectroscopy and Related Phenomena, 3(3):217–226, 1974.
- [26] Atsushi Fujimori, M Saeki, N Kimizuka, M Taniguchi, and S Suga. Photoemission satellites and electronic structure of $\text{fe } 2\text{ o } 3$. Physical Review B, 34(10):7318, 1986.
- [27] Supriyo Majumder, P Basera, Malvika Tripathi, RJ Choudhary, S Bhattacharya, K Bapna, and DM Phase. Elucidating the origin of magnetic ordering in ferroelectric batio_3 -d thin film via electronic structure modification. Journal of Physics: Condensed Matter, 31(20):205001, 2019.
- [28] NE Brese and M O’keeffe. Bond-valence parameters for solids. Structural Science, 47(2):192–197, 1991.
- [29] I David Brown. The chemical bond in inorganic chemistry: the bond valence model, volume 27. Oxford university press, 2016.
- [30] Arvind Kumar Yogi, Alexander Yaresko, CI Sathish, Hasung Sim, Daisuke Morikawa, Juergen Nuss, Kenji Tsuda, Yukio Noda, Daniel I Khomskii, and Je-Geun Park. Coexisting z-type charge and bond order in metallic naru_2o_4 . Communications Materials, 3(1):3, 2022.
- [31] Ganesh Bera, Akash Surampalli, Maximiliano L Riddick, V Raghavendra Reddy, VG Sathe, GR Turpu, Edmund Welter, Archana Sagdeo, and Carlo Meneghini. Local structural investigation across the magnetic transition in the type-ii multiferroic material fevo_4 . Physical Review B, 109(7):075138, 2024.
- [32] Maurizio Benfatto and Carlo Meneghini. A close look into the low energy region of the xas spectra: the xanes region. In Synchrotron Radiation: Basics, Methods and Applications, pages 213–240. Springer, 2014.
- [33] C Meneghini, F Bardelli, and S Mobilio. Estra-fitexa: a software package for exafs data analysis. Nuclear Instruments and Methods in Physics Research Section B: Beam Interactions with Materials and Atoms, 285:153–157, 2012.
- [34] Diek C Koningsberger and Roelof Prins. X-ray absorption: principles, applications, techniques of exafs, sexafs and xanes. 1987.
- [35] Takashi Yamamoto. Assignment of pre-edge peaks in k-edge x-ray absorption spectra of 3d transition metal compounds: electric dipole or quadrupole? X-Ray Spectrometry: An International Journal, 37(6):572–584,

- 2008.
- [36] ZY Wu, DC Xian, TD Hu, YN Xie, Y Tao, CR Natoli, Eleonora Paris, and A Marcelli. Quadrupolar transitions and medium-range-order effects in metal k-edge x-ray absorption spectra of 3 d transition-metal compounds. Physical Review B—Condensed Matter and Materials Physics, 70(3):033104, 2004.
- [37] Ajay Kumar, Rishabh Shukla, Ravi Kumar, RJ Choudhary, SN Jha, and RS Dhaka. Probing the electronic and local structure of sr 2- x la x conbo 6 using near-edge and extended x-ray absorption fine structures. Physical Review B, 105(24):245155, 2022.
- [38] P Glatzel, M Sikora, and M Fernandez-Garcia. Resonant x-ray spectroscopy to study k absorption pre-edges in 3d transition metal compounds. The European Physical Journal Special Topics, 169(1):207–214, 2009.
- [39] CR Natoli. Distance dependence of continuum and bound state of excitonic resonances in x-ray absorption near edge structure (xanes). In EXAFS and Near Edge Structure III: Proceedings of an International Conference, Stanford, CA, July 16–20, 1984, pages 38–42. Springer, 1984.
- [40] Aline Y Ramos, Hélio CN Tolentino, Narcizo M Souza-Neto, Jean-Paul Itié, Liliana Morales, and Alberto Caneiro. Stability of jahn-teller distortion in lamno3 under pressure: direct study by x-ray absorption. arXiv preprint cond-mat/0701759.
- [41] N Ishimatsu, T Watanabe, K Oka, M Azuma, M Mizumaki, K Nitta, T Ina, and N Kawamura. Differences in local structure around co and fe of the bico 1- x fe x o 3 system determined by x-ray absorption fine structure. Physical Review B, 92(5):054108, 2015.
- [42] Adriano Filipponi, Andrea Di Cicco, and Calogero Renzo Natoli. X-ray-absorption spectroscopy and n-body distribution functions in condensed matter. i. theory. Physical Review B, 52(21):15122, 1995.
- [43] Grant Bunker. Introduction to XAFS: a practical guide to X-ray absorption fine structure spectroscopy. Cambridge University Press, 2010.
- [44] Marco Vaccari and Paolo Fornasini. Einstein and debye models for exafs parallel and perpendicular mean-square relative displacements. Journal of synchrotron radiation, 13(4):321–325, 2006.
- [45] S Basu, C Nayak, AK Yadav, A Agrawal, AK Poswal, D Bhattacharyya, SN Jha, and NK Sahoo. A comprehensive facility for exafs measurements at the indus-2 synchrotron source at rrcat, indore, india. In Journal of Physics: Conference Series, volume 493, page 012032. IOP Publishing, 2014.
- [46] Dibya Phuyal, Soham Mukherjee, Swarup K Panda, Gabriel J Man, Konstantin Simonov, Laura Simonelli, Sergei M Butorin, Håkan Rensmo, and Olof Karis. Nonlocal interactions in the double perovskite sr2femoo6 from core-level x-ray spectroscopy. The Journal of Physical Chemistry C, 125(20):11249–11256, 2021.
- [47] Isaac B Bersuker. Electronic structure and properties of transition metal compounds: introduction to the theory. John Wiley & Sons, 2010.
- [48] Roger G Burns. Mineralogical applications of crystal field theory. Number 5. Cambridge university press, 1993.
- [49] YH Hou, YJ Zhao, ZW Liu, HY Yu, XC Zhong, WQ Qiu, DC Zeng, and LS Wen. Structural, electronic and magnetic properties of partially inverse spinel cofe2o4: a first-principles study. Journal of Physics D: Applied Physics, 43(44):445003, 2010.
- [50] GA Sawatzky, F Van Der Woude, and AH Morrish. Mössbauer study of several ferrimagnetic spinels. Physical Review, 187(2):747, 1969.
- [51] Frank Edward Mabbs and David John Machin. Magnetism and transition metal complexes. Courier Corporation, 2008.
- [52] Francesc Lloret, Miguel Julve, Joan Cano, Rafael Ruiz-García, and Emilio Pardo. Magnetic properties of six-coordinated high-spin cobalt (ii) complexes: Theoretical background and its application. Inorganica Chimica Acta, 361(12-13):3432–3445, 2008.
- [53] Huimei Liu and Giniyat Khaliullin. Pseudospin exchange interactions in d 7 cobalt compounds: Possible realization of the kitaev model. Physical Review B, 97(1):014407, 2018.
- [54] György Vankó, Jean-Pascal Rueff, Alekski Mattila, Zoltán Németh, and Abhay Shukla. Temperature-and pressure-induced spin-state transitions in laco 3. Physical Review B—Condensed Matter and Materials Physics, 73(2):024424, 2006.
- [55] AE Bocquet, T Mizokawa, T Saitoh, H Namatame, and A Fujimori. Electronic structure of 3d-transition-metal compounds by analysis of the 2p core-level photoemission spectra. Physical Review B, 46(7):3771, 1992.
- [56] SP Kowalczyk, L Ley, RA Pollak, FR McFeely, and DA Shirley. New multiplet structure in photomission from mn f 2. Physical Review B, 7(8):4009, 1973.
- [57] S Hüfner and GK Wertheim. Core-electron splittings and hyperfine fields in transition-metal compounds. Physical Review B, 7(6):2333, 1973.
- [58] JC Carver, GK Schweitzer, and Thomas A Carlson. Use of x-ray photoelectron spectroscopy to study bonding in cr, mn, fe, and co compounds. The Journal of Chemical Physics, 57(2):973–982, 1972.
- [59] AE Bocquet, T Mizokawa, K Morikawa, A Fujimori, SR Barman, K Maiti, DD Sarma, Y Tokura, and M Onda. Electronic structure of early 3d-transition-metal oxides by analysis of the 2p core-level photoemission spectra. Physical Review B, 53(3):1161, 1996.
- [60] L Sangaletti, Laura Eleonora Depero, PS Bagus, and Fulvio Parmigiani. A proper anderson hamiltonian treatment of the 3s photoelectron spectra of mno, feo, coo and nio. Chemical physics letters, 245(4-5):463–468, 1995.
- [61] Mahnaz Ghiasi, Atsushi Hariki, Mathias Winder, Jan Kuneš, Anna Regoutz, Tien-Lin Lee, Yongfeng Hu, Jean-Pascal Rueff, and Frank MF De Groot. Charge-transfer effect in hard x-ray 1 s and 2 p photoemission spectra: Lda+ dmft and cluster-model analysis. Physical Review B, 100(7):075146, 2019.
- [62] Supriyo Majumder, Malvika Tripathi, R Raghunathan, P Rajput, SN Jha, DO De Souza, L Olivi, S Chowdhury, RJ Choudhary, and DM Phase. Mapping the magnetic state as a function of antisite disorder in sm 2 nimno 6 double perovskite thin films. Physical Review B, 105(2):024408, 2022.
- [63] RP Gupta and SK Sen. Calculation of multiplet structure of core p-vacancy levels. ii. Physical Review B, 12(1):15, 1975.
- [64] A Rosencwaig, GK Wertheim, and HJ Guggenheim. Origins of satellites on inner-shell photoelectron spectra. Physical Review Letters, 27(8):479, 1971.
- [65] G Hu, JH Choi, CB Eom, VG Harris, and Y Suzuki. Structural tuning of the magnetic behavior in spinel-

- structure ferrite thin films. Physical Review B, 62(2):R779, 2000.
- [66] AFL Moreira, FLO Paula, AFC Campos, and J Depeyrot. Local structure investigation of cobalt ferrite-based nanoparticles by synchrotron x-ray diffraction and absorption spectroscopy. Journal of Solid State Chemistry, 286:121269, 2020.
- [67] Bhavna C Keswani, SI Patil, YD Kolekar, and CV Ravana. Improved magnetostrictive properties of cobalt ferrite (cofe₂o₄) by mn and dy co-substitution for magneto-mechanical sensors. Journal of Applied Physics, 126(17), 2019.
- [68] Jose-Luis Ortiz-Quiñonez, Umapada Pal, and Martin Salazar Villanueva. Structural, magnetic, and catalytic evaluation of spinel co, ni, and co-ni ferrite nanoparticles fabricated by low-temperature solution combustion process. ACS omega, 3(11):14986–15001, 2018.
- [69] Alexei Kuzmin and Jesús Chaboy. Exafs and xanes analysis of oxides at the nanoscale. IUCrJ, 1(6):571–589, 2014.
- [70] AM Mulders, SM Lawrence, U Staub, M Garcia-Fernandez, V Scagnoli, Claudio Mazzoli, E Pomjakushina, K Conder, and Y Wang. Direct observation of charge order and an orbital glass state in multiferroic lufe₂o₄. Physical review letters, 103(7):077602, 2009.